Supporting Information:

# Co and Mo co-doped $Fe_2O_3$ for Selective Ethylene Production via Chemical Looping Oxidative Dehydrogenation

Xin Tian[1], Chaohe Zheng[1], Fanxing Li[2, *], Haibo Zhao[1, *]

[1] State Key Laboratory of Coal Combustion, School of Energy and Power Engineering, Huazhong University of Science and Technology, Luoyu Road 1037#, Hongshan District, Wuhan 430074, PR China
[2] Department of Chemical & Biomolecular Engineering, North Carolina State University, 911 Partners Way, Raleigh, NC 27695-7905 USA

[*] Email: fli5@ncsu.edu; hzhao@mail.hust.edu.cn

This document provides additional information on data evaluation, reaction data, redox catalyst characterizations, DFT calculation details and results.

Total number of Pages: 20

Total number of Figures: 10

Total number of Tables: 8

**Part S1: Reaction Testing and Characterization Results**

➢ *Data Evaluation*

All the carbonaceous species are normalized to $C_2$ during the data analysis, and $n(X)$ in the formulas below refers to the total amount of carbonaceous species $X$ measured in tail gas.

- The $C_2H_6$ conversion is calculated as,

$$C_2H_6 \text{ conversion} = 1 - \frac{n(C_2H_6)}{n(\text{Total carbonaceous species})} \quad \text{(s1)}$$

- The product selectivity to carbonaceous species $X$ is calculated as,

$$\text{Selectivity to carbonaceous species } X = \frac{n(X)}{n(\text{Total carbonaceous species}) - n(C_2H_6)} \quad \text{(s2)}$$

- The yield of carbonaceous species $X$ is calculated as,

$$\text{Yield of carbonaceous species } X = (C_2H_6 \text{ conversion}) * (\text{Selectivity to } X) \quad \text{(s3)}$$

- The $H_2$ conversion is calculated as,

$$H_2 \text{ conversion} = 1 - \frac{n(H_2)}{n(\text{Total } H_2 \text{ generated})} \quad \text{(s4)}$$

- The amount of lattice oxygen donated by the redox catalyst during the reaction is calculated as,

$$O_2 \text{ donation} = n(CO) + 2\,n(CO_2) + n(H_2O) \quad \text{(s5)}$$

**Table S1** ICP-OES results for the prepared $Mo/Fe_2O_3$, $Co_{0.3}Mo_{0.7}/Fe_2O_3$, and $CoFe_2O_4$ samples.

| Samples | Molar ratio (%) | | |
|---|---|---|---|
| | Co | Mo | Fe |
| $Mo/Fe_2O_3$ | - | 6.5 | 93.5 |
| $Co_{0.3}Mo_{0.7}/Fe_2O_3$ | 12.6 | 8.7 | 78.7 |
| $CoFe_2O_4$ | 32.9 | - | 67.1 |

**Table S2** Supplemental reaction data for five redox catalysts as well as thermal blank at GHSV = 6000 $h^{-1}$ and T = 775°C to 825°C. Accompanying **Figure 3** of **Results and Discussion**.

| Samples | T (°C) | $C_2H_6$ Conv. (%) | $C_2H_4$ Select. (%) | $CH_4$ Select. (%) | $CO_x$ Select. (%) | $H_2$ Conv. (%) |
|---|---|---|---|---|---|---|
| | 775 | 14.91 | 83.92 | 16.08 | - | - |
| $Al_2O_3$ (blank) | 800 | 29.37 | 89.02 | 10.98 | - | - |
| | 825 | 46.99 | 90.60 | 9.40 | - | - |
| | 775 | 58.05 | 26.53 | 1.40 | 72.08 | 99.40 |
| $CoFe_2O_4$ | 800 | 69.95 | 19.40 | 1.28 | 79.32 | 99.93 |
| | 825 | 82.94 | 15.59 | 1.07 | 83.34 | 99.35 |
| | 775 | 21.92 | 42.21 | 12.24 | 45.55 | 91.60 |
| $Co_{0.4}Mo_{0.6}/Fe_2O_3$ | 800 | 36.57 | 64.44 | 4.87 | 30.69 | 89.78 |
| | 825 | 58.99 | 40.52 | 4.60 | 54.88 | 96.69 |
| | 775 | 20.24 | 83.04 | 11.36 | 5.60 | 79.70 |
| $Co_{0.3}Mo_{0.7}/Fe_2O_3$ | 800 | 38.49 | 89.67 | 6.65 | 3.68 | 86.96 |
| | 825 | 56.19 | 87.42 | 5.99 | 6.59 | 90.78 |
| | 775 | 17.09 | 80.49 | 12.29 | 7.22 | 92.24 |
| $Co_{0.2}Mo_{0.8}/Fe_2O_3$ | 800 | 31.65 | 85.73 | 7.35 | 6.91 | 96.16 |
| | 825 | 57.36 | 78.10 | 6.73 | 15.17 | 98.03 |
| | 775 | 18.49 | 81.58 | 12.58 | 5.84 | 42.96 |
| $Mo/Fe_2O_3$ | 800 | 33.01 | 87.17 | 9.66 | 3.17 | 39.47 |
| | 825 | 52.28 | 85.87 | 7.59 | 6.55 | 27.18 |

**Table S3** Ethane conversion, carbonaceous gas products selectivity, and $H_2$ conversion of $Co_{0.3}Mo_{0.7}/Fe_2O_3$ during the reaction with ethane at different ethane feeding durations: feeding gas composition, 5 mL/min $C_2H_6$ + 35 mL/min Ar; reaction temperature, 800 ºC; sample weight, 700 mg.

| Samples | Reaction duration | $C_2H_6$ Con. (%) | $C_2H_4$ Select. (%) | $CH_4$ Select. (%) | $CO_x$ Select. (%) | $H_2$ Con. (%) |
|---|---|---|---|---|---|---|
| $Al_2O_3$ (blank) | 1.0 min | 29.37 | 89.02 | 10.98 | - | - |
| $Co_{0.3}Mo_{0.7}/Fe_2O_3$ | 1.0 min | 38.49 | 89.67 | 6.65 | 3.68 | 86.96 |
| $Co_{0.3}Mo_{0.7}/Fe_2O_3$ | 2.0 min | 36.55 | 90.34 | 6.70 | 2.96 | 84.66 |
| $Co_{0.3}Mo_{0.7}/Fe_2O_3$ | 2.5 min | 35.48 | 82.13 | 8.46 | 9.40 | 82.51 |

**Table S4** Reduction onset temperature and highly selective (over 85% ethylene selectivity) temperature range of redox catalysts / thermal blank as determined by $C_2H_6$-TPR.

| Samples | Onset Tem. (ºC) | Selective Tem. range (ºC) |
|---|---|---|
| $Al_2O_3$ (blank) | 730 | 730 – 850 |
| $CoFe_2O_4$ | 623 | 623 – 650 |
| $Co_{0.3}Mo_{0.7}/Fe_2O_3$ | 722 | 722 – 830 |
| $Mo/Fe_2O_3$ | 709 | 709 – 820 |

**Table S5** Near-surface cation atomic percentages for the cycled $Co_{0.3}Mo_{0.7}/Fe_2O_3$ (5 redox cycles, samples collected at oxidation state) with different ethane reaction durations (1 min, 2 min, and 2.5 min).

| Reaction duration | Atomic percentage | | |
|---|---|---|---|
| | Co 2*p* | Mo 3*d* | Fe 2*p* |
| 1 min | 29.0% | 29.6% | 41.4% |
| 2 min | 23.8% | 21.5% | 54.7% |
| 2.5 min | 23.9% | 18.6% | 57.4% |

**Table S6** The analysis results of Fe $2p_{3/2}$, Mo $3d_{5/2}$, Co $2p_{3/2}$, and O 1*s* XPS spectra for the $Mo/Fe_2O_3$, $CoFe_2O_4$, and $Co_{0.3}Mo_{0.7}/Fe_2O_3$ redox catalysts.

| Samples | Spectrum | B.E. (eV) | Assignment | Atomic percentage |
|---|---|---|---|---|
| $Mo/Fe_2O_3$ | Fe $2p_{3/2}$ | 709.66 | $Fe^{2+}$ | 9.0% |
| | | 710.80 | $Fe^{3+}$ | 44.5% |
| | | 713.01 | $Fe^{3+}$ | 46.5% |
| | Mo $3d_{5/2}$ | 231.22 | $Mo^{3+}$ | 8.1% |
| | | 232.42 | $Mo^{4+}$ | 84.1% |
| | | 232.69 | $Mo^{4+}$ | 7.8% |
| | O 1*s* | 529.40 | lattice O | 42.5% |
| | | 530.01 | electrophilic surface O | 5.2% |
| | | 531.51 | $OH^-$ species | 31.3% |
| | | 532.81 | absorbed $H_2O$ | 21.0% |
| $Co_{0.3}Mo_{0.7}/Fe_2O_3$ | Fe $2p_{3/2}$ | 709.57 | $Fe^{2+}$ | 26.6% |
| | | 710.61 | $Fe^{3+}$ | 39.8% |
| | | 713.00 | $Fe^{3+}$ | 33.6% |
| | Mo $3d_{5/2}$ | 230.70 | $Mo^{3+}$ | 3.9% |
| | | 232.00 | $Mo^{4+}$ | 59.5% |
| | | 232.68 | $Mo^{4+}$ | 36.6% |
| | Co $2p_{3/2}$ | 779.87 | $Co^{2+}$ | 37.4% |
| | | 782.70 | $Co^{2+}$ | 33.6% |
| | | 786.82 | $Co^{3+}$ | 29.0% |
| | O 1*s* | 529.32 | lattice O | 64.1% |
| | | 530.35 | electrophilic surface O | 4.3% |
| | | 531.15 | $OH^-$ species | 17.0% |
| | | 532.66 | absorbed $H_2O$ | 14.6% |
| $CoFe_2O_4$ | Fe $2p_{3/2}$ | 709.71 | $Fe^{2+}$ | 8.5% |
| | | 710.73 | $Fe^{3+}$ | 35.7% |
| | | 713.06 | $Fe^{3+}$ | 55.8% |
| | Co $2p_{3/2}$ | 779.70 | $Co^{2+}$ | 17.8% |
| | | 781.41 | $Co^{2+}$ | 50.1% |
| | | 786.59 | $Co^{3+}$ | 32.1% |
| | O 1*s* | 529.63 | lattice O | 30.64% |
| | | 529.90 | electrophilic surface O | 39.25% |
| | | 531.29 | $OH^-$ species | 26.54% |
| | | 533.30 | absorbed $H_2O$ | 3.58% |

**Table S7** BET surface area for the cycled $Mo/Fe_2O_3$, $Co_{0.3}Mo_{0.7}/Fe_2O_3$, and $CoFe_2O_4$.

| Samples | Surface area ($m^2g^{-1}$) | Pore volume ($cm^3g^{-1}$) | Pore size (nm) |
|---|---|---|---|
| $Mo/Fe_2O_3$ | 105.3901 | 0.3225 | 9.5413 |
| $Co_{0.3}Mo_{0.7}/Fe_2O_3$ | 126.2047 | 0.2671 | 9.5938 |
| $CoFe_2O_4$ | 94.7952 | 0.5184 | 12.5131 |

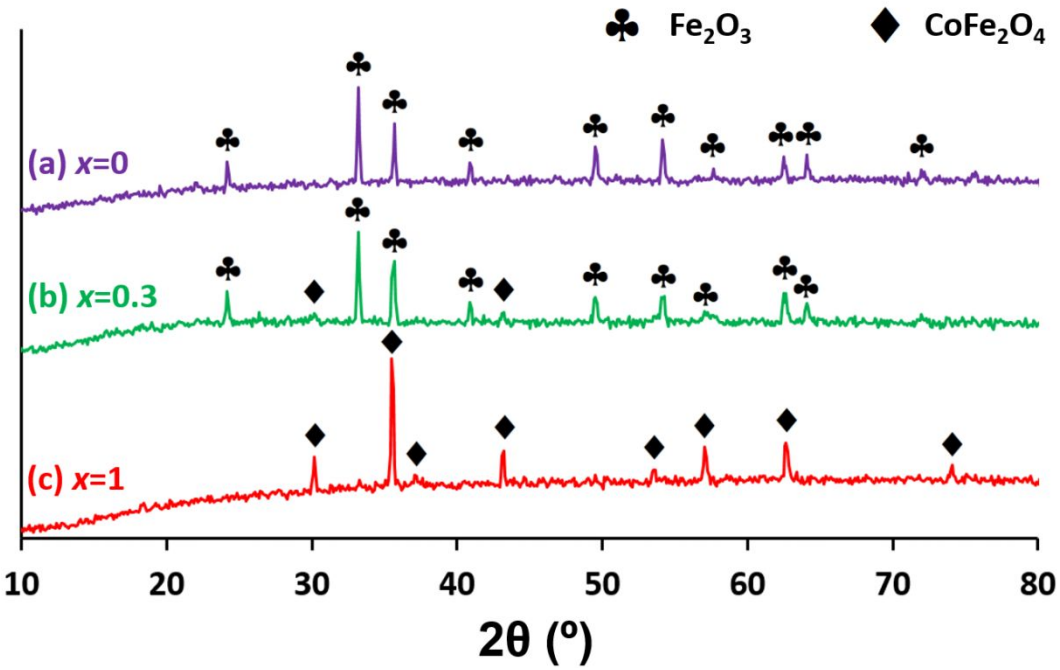


**Figure S1** XRD patterns for the cycled $Co_xMo_{1-x}/Fe_2O_3$ ($x$ = 0, 0.3, 1) samples: (a) $Mo/Fe_2O_3$, (b) $Co_{0.3}Mo_{0.7}/Fe_2O_3$, and (c) $CoFe_2O_4$.

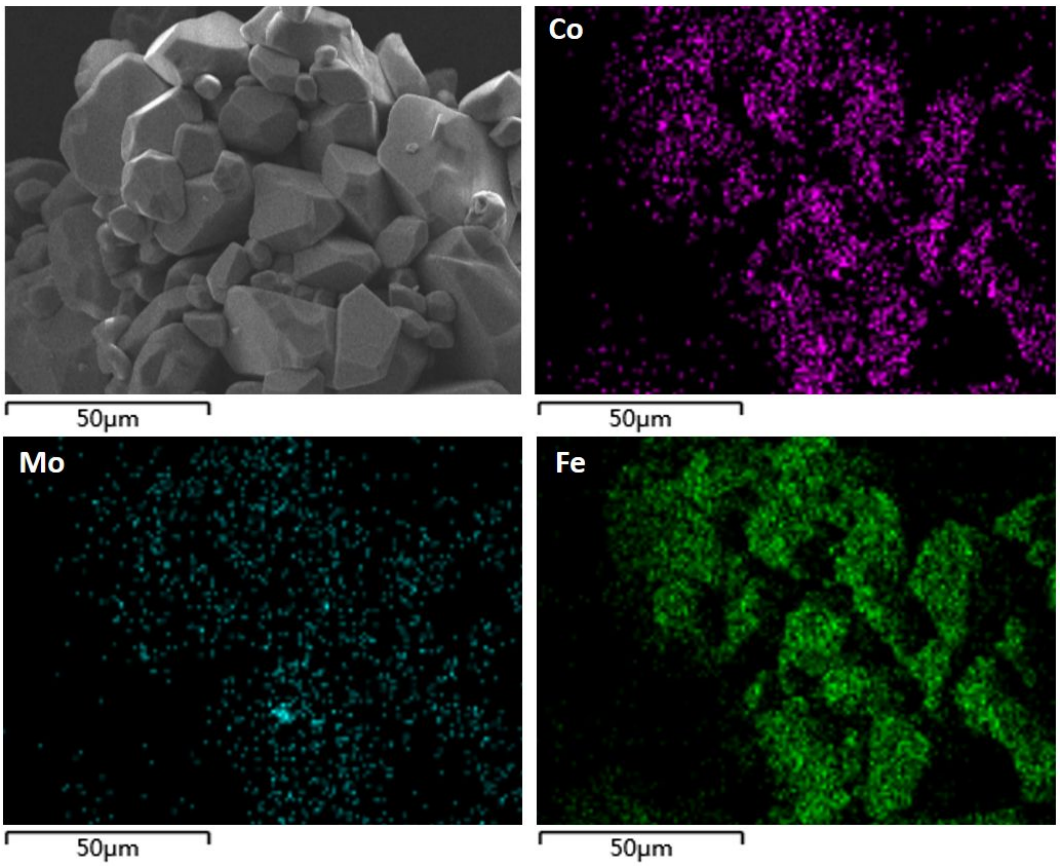


**Figure S2** The SEM image and EDS mapping for the fresh $Co_{0.3}Mo_{0.7}/Fe_2O_3$ redox catalysts.

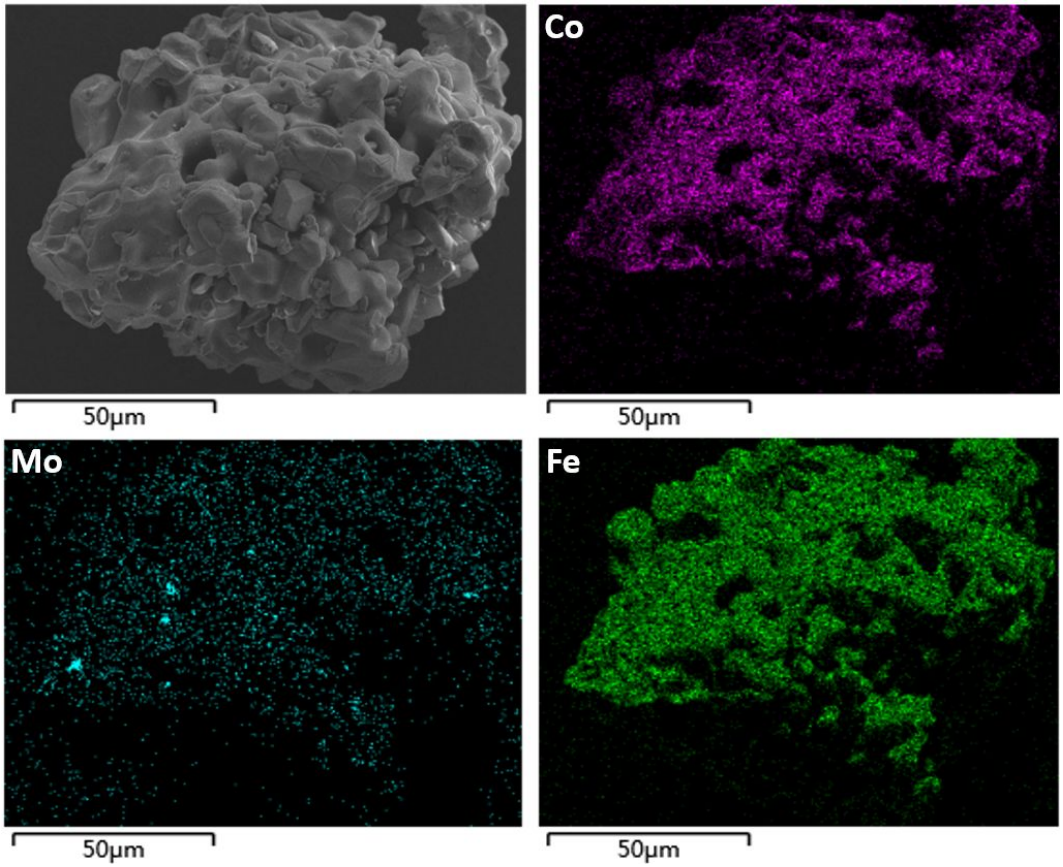


**Figure S3** The SEM image and EDS mapping for the cycled $Co_{0.3}Mo_{0.7}/Fe_2O_3$ redox catalysts.

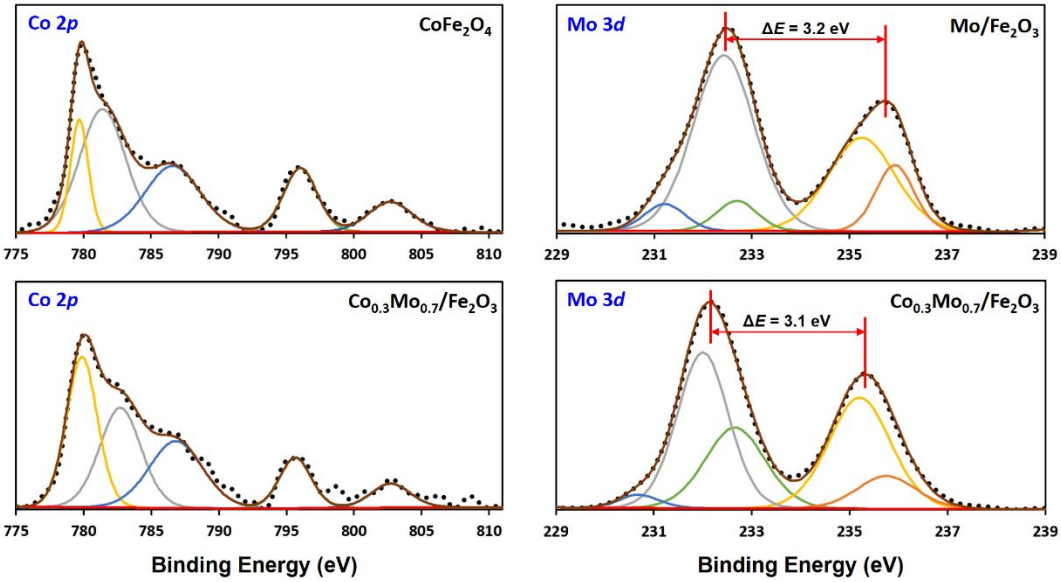


**Figure S4** Co 2*p* and/or Mo 3*d* XPS spectra for the $CoFe_2O_4$, $Mo/Fe_2O_3$, and $Co_{0.3}Mo_{0.7}/Fe_2O_3$ redox catalysts (in oxidation state).

**Part S2: DFT Calculation Details and Results**

*S2.1 Model construction*

The $CoFe_2O_4$ lattice cell and (100) slab model are constructed and shown in **Figure S5**. As it can be seen in **Figure S5a**, the crystal structure of $CoFe_2O_4$ energetically favors the inverse spinel structure, which consists of 8 Co atoms, 16 Fe atoms, and 32 O atoms. Half of the octahedral sites are occupied by $Co^{2+}$ cations, while the other half of the octahedral site and all of the tetrahedral sites are occupied by $Fe^{3+}$ cations [1]. The spin arrangement of up-spin directions represents the tetrahedral site Fe atoms, and that of down-spin directions denotes the octahedral site Fe and Co atoms [1, 2]. After geometry optimization, the calculated lattice parameters for the $CoFe_2O_4$ cell are a = b = 8.40 Å and c = 8.37 Å, which agree well with previous experimental values (a = b = 8.38 Å, c = 8.31 Å) [3]. With these in mind, a nine-layer slab model with a vacuum space of 15 Å is constructed for the $CoFe_2O_4$(100) surface, where the top five layers are relaxed and bottom four layers are fixed. The side view and top view of $CoFe_2O_4$(100) surface slab are shown in **Figure S5b** and **c**, respectively.

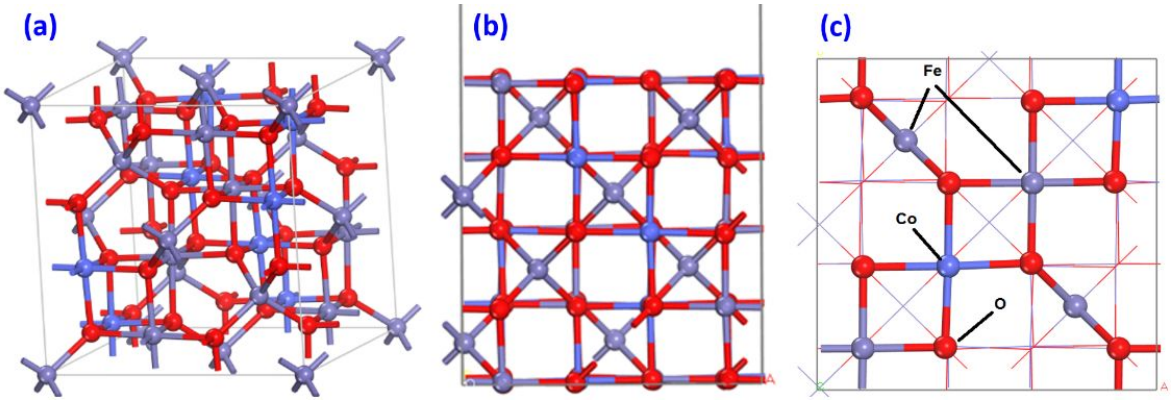


**Figure S5** (a) $CoFe_2O_4$ cell, (b) side view, and (c) top view for the $CoFe_2O_4$(100) surface slab.

We note here that the prepared $Mo/Fe_2O_3$ and $Co_{0.3}Mo_{0.7}/Fe_2O_3$ redox catalysts possess a supported-type structure, which make it difficult to construct a cell model in DFT that is exactly the same as the real crystal structure of the sample [4]. As a compromise, spinel-structured $MoFe_2O_4$ and $Co_{1/4}Mo_{3/4}Fe_2O_4$ are constructed and used as cell models for $Mo/Fe_2O_3$ and $Co_{0.3}Mo_{0.7}/Fe_2O_3$, respectively, in DFT calculations. For the $Mo/Fe_2O_3$ redox catalyst, a $MoFe_2O_4$ cell with the antiferromagnetic spin arrangement is constructed (**Figure S6**), which consists of 8 Mo atoms, 16 Fe atoms, and 32 O atoms [5]. Half of the octahedral sites are occupied by Mo cations, and the other half of the octahedral site and all of the tetrahedral sites are occupied by Fe cations. The spin arrangement of up-spin directions represents the tetrahedral site Fe atoms, and that of down-spin directions denotes the octahedral site Fe and Mo atoms. As shown in **Fig. S6a**, the

calculated lattice parameters of the $MoFe_2O_4$ cell are a = b = c = 8.57 Å, which are consistent with previous experimental values (a = b = c = 8.51 Å) [6]. Finally, a nine-layer slab model is constructed for the $MoFe_2O_4$(100) surface, with a vacuum space of 15 Å. **Figure S6b** and **c** shows the side view and top view of the $CoFe_2O_4$(100) surface slab, respectively.

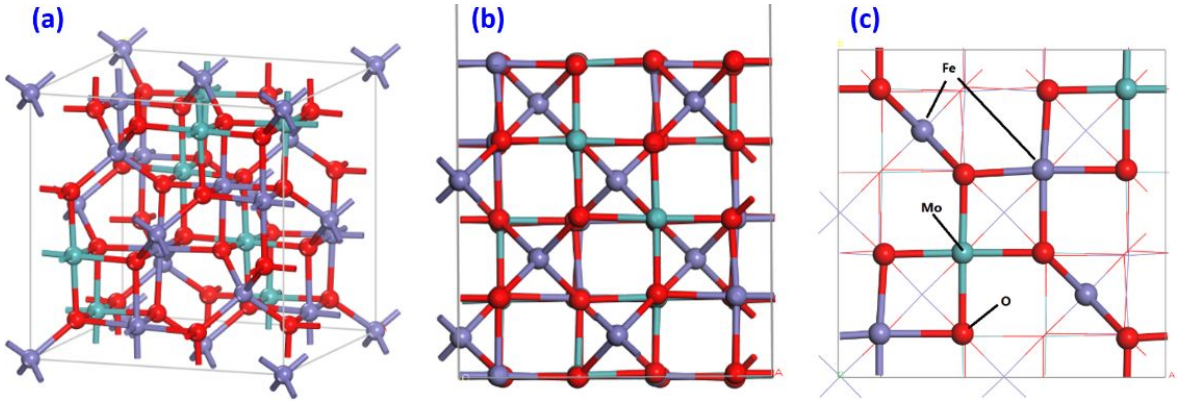


**Figure S6** (a) $MoFe_2O_4$ cell, (b) side view, and (c) top view for the $MoFe_2O_4$(100) surface slab.

With respect to the $Co_{0.3}Mo_{0.7}/Fe_2O_3$ redox catalyst, a $Co_{1/4}Mo_{3/4}Fe_2O_4$ cell with the antiferromagnetic spin arrangement is constructed by partial substitution of Mo with Co in the $MoFe_2O_4$ lattice. We note here that there are only 8 Mo atoms in the constructed $MoFe_2O_4$ cell, thus it is infeasible to build a lattice cell with a Co/Mo molar ratio of 0.3:0.7 (corresponding to 2.4 Co atoms and 5.6 Mo atoms) exactly in DFT. In order to closely match the molar ratio of different elements in $Co_{0.3}Mo_{0.7}/Fe_2O_3$, a $Co_{1/4}Mo_{3/4}Fe_2O_4$ cell with the antiferromagnetic spin arrangement is constructed (**Figure S7**), which consists of 2 Co atoms, 6 Mo atoms, 16 Fe atoms, and 32 O atoms. As shown in **Figure S7a**, the two Co cations in the $Co_{1/4}Mo_{3/4}Fe_2O_4$ cell are marked with brown circles. The calculated lattice parameters for the $Co_{1/4}Mo_{3/4}Fe_2O_4$ cell (a = b =8.53 Å, c = 8.46 Å) are close to the $MoFe_2O_4$ cell (a = b = c = 8.57 Å). Finally, a nine-layer slab model is constructed for the $Co_{1/4}Mo_{3/4}Fe_2O_4$(100) surface.

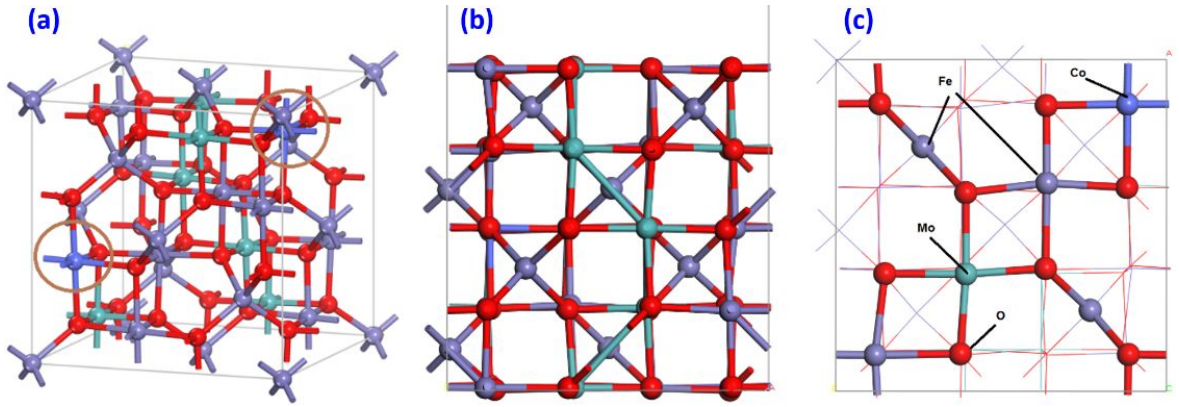


**Figure S7** (a) $Co_{1/4}Mo_{3/4}Fe_2O_4$ cell, (b) side view, and (c) top view for the $Co_{1/4}Mo_{3/4}Fe_2O_4$(100) surface slab.

*S2.2 Formulas used in DFT calculation*

The adsorption energy ($E_{ads}$) is expressed as:

$$E_{ads} = E(\text{slab@ethane}) - E(\text{ethane}) - E(\text{slab}) \quad \text{(s6)}$$

where $E$(slab@ethane) and $E$(slab) represent the total energy of the adsorption structure and the substrate slab of $CoFe_2O_4$, $MoFe_2O_4$, or $Co_{1/4}Mo_{3/4}Fe_2O_4$, respectively; $E$(ethane) represents the total energy of gaseous ethane.

The oxygen vacancy formation energy is computed according to the following formula:

$$E_{O_v} = E(\text{slab@}O_v) + 1/2\,E(O_2) - E(\text{slab}) \quad \text{(s7)}$$

where $E$(slab@$O_v$) is the total energy of the slab model containing oxygen vacancy; $E$($O_2$) is the total energy of $O_2$ molecule; $E$(slab) represents the total energy of initial stoichiometric slab model of $CoFe_2O_4$, $MoFe_2O_4$, or $Co_{1/4}Mo_{3/4}Fe_2O_4$.

The activation free energy $E_b$ is calculated as:

$$E_b = E(\text{TS}) - E(\text{IS}) \quad \text{(s8)}$$

where $E$(TS) and $E$(IS) are the total energy of the transition state and the initial state, respectively, and the transition state is calculated by the linear/quadratic synchronous transit (LST/QST) method.

*S2.3 Surface adsorption*

The optimized geometric structures of ethane adsorption on the surfaces of $CoFe_2O_4$, $MoFe_2O_4$, and $Co_{1/4}Mo_{3/4}Fe_2O_4$ are shown in **Figure S8**. For the stoichiometric $CoFe_2O_4$ surface, the optimal adsorption configuration is the one that ethane adsorbs in parallel to the bridge site between Fe and Co atoms (**Figure S8a**). As summarized in **Table S8**, the adsorption energy for the $CoFe_2O_4$ adsorption configuration is -45.78 kJ/mol and the equilibrium distance of C-H bond is 1.106 Å. The C-H bond equilibrium distance is slightly higher than that of the free ethane molecule (1.100 Å), indicating that the adsorption of ethane on the $CoFe_2O_4$ surface would weaken the interaction between C and H atoms. In other words, the adsorption of ethane might promote oxidative C-H bond cleavage to some extent. With respect to $MoFe_2O_4$ and $Co_{1/4}Mo_{3/4}Fe_2O_4$ surfaces, the optimal adsorption configurations are both the one that ethane adsorbs in parallel to the bridge site between Fe and Mo atoms, and the adsorption energies are -44.23 kJ/mol and -45.78 kJ/mol, respectively. The calculated adsorption energies suggest that ethane adsorption on the $MoFe_2O_4$ surface might be a reversible physisorption (< 0.4 eV), whereas that for $CoFe_2O_4$ and $Co_{0.3}Mo_{0.7}Fe_2O_4$ are irreversible chemisorption (> 0.4 eV) [7]. In addition, the C-H bond length on the three surfaces follows the order of $CoFe_2O_4$ > $Co_{1/4}Mo_{3/4}Fe_2O_4$ > $MoFe_2O_4$, which indicates that the activation of ethane (namely the $C_2H_6$ initial dehydrogenation) on the $CoFe_2O_4$ surface is the easiest.

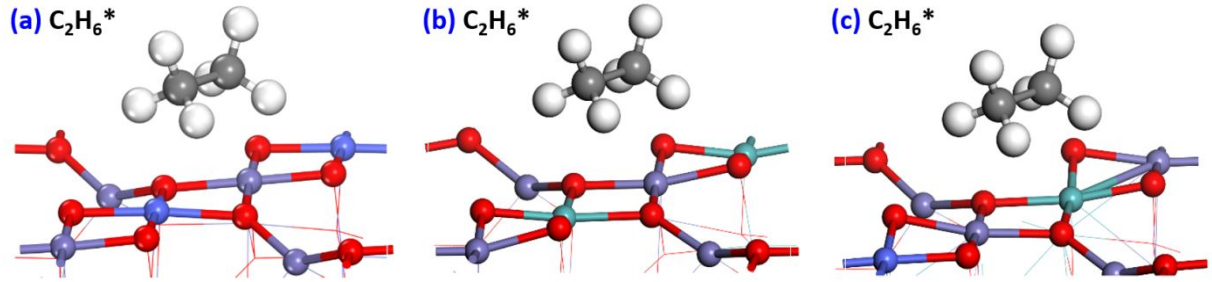


**Figure S8** The optimized geometric structures of ethane adsorption on the surface of (a) $CoFe_2O_4$, (b) $MoFe_2O_4$, and (c) $Co_{1/4}Mo_{3/4}Fe_2O_4$, respectively.

**Table S8** The bond length, adsorption energy, and charge transfer of ethane adsorption on the surfaces of $CoFe_2O_4$, $MoFe_2O_4$, and $Co_{1/4}Mo_{3/4}Fe_2O_4$.

| Models | C-Co(Mo)/Å | C-Fe/Å | C-C/Å | C-H/Å | $E_{ads}$/ kJ·mol$^{-1}$ | Q/*e* |
|---|---|---|---|---|---|---|
| $CoFe_2O_4$ | 2.864 | 2.927 | 1.534 | 1.106 | -45.78 | -0.41 |
| $MoFe_2O_4$ | 3.199 | 3.110 | 1.535 | 1.103 | -38.29 | -0.31 |
| $Co_{1/4}Mo_{3/4}Fe_2O_4$ | 3.059 | 3.000 | 1.534 | 1.104 | -44.23 | -0.33 |

*S2.4 Successive dissociation*

The potential energy profiles of $C_2H_6$ successive dehydrogenation on different surfaces are shown in **Figure S9**, and the corresponding structures at different steps are present in **Figure S10**. Ethane is adsorbed on the surface and then oxidized by a three-coordinated lattice oxygen to produce ethylene. The activation free energies for the first (155.49 kJ/mol) and second (149.61 kJ/mol) oxidative C-H bond cleavage on the $MoFe_2O_4$ surface are higher than those on $CoFe_2O_4$ surface (125.66 and 126.33 kJ/mol) and $Co_{1/4}Mo_{3/4}Fe_2O_4$ surface (130.38 and 132.80 kJ/mol). These results indicate that the Co atom can significantly reduce the activation free energy of C-H bond cleavage and thus facilitate ethane dehydrogenation. This point can be confirmed by the experimental results shown in **Figure 3** of the main text, that the ethane conversion under the same condition follow the order of $CoFe_2O_4$ > $Co_{0.3}Mo_{0.7}/Fe_2O_3$ > $Mo/Fe_2O_3$.

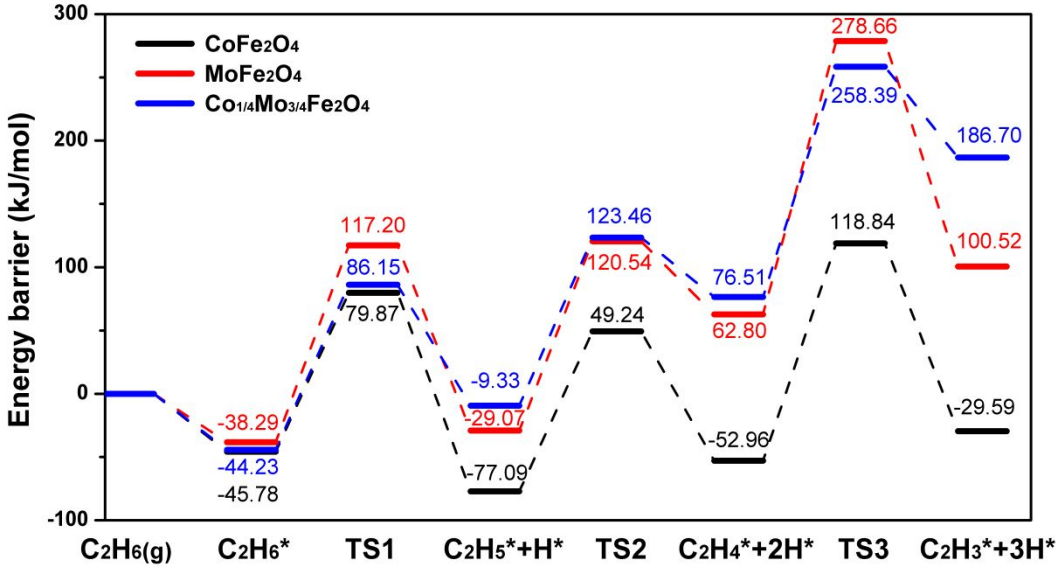


**Figure S9** Potential energy profiles of ethane successive dehydrogenation (including the overly oxidative C-H bond cleavage step, TS3) on the surface of $CoFe_2O_4$, $MoFe_2O_4$, and $Co_{1/4}Mo_{3/4}Fe_2O_4$, respectively.

The oxidative C-C bond cleavage of $H_3C$-$CH_3$ and $H_2C$=$CH_2$ are also examined in DFT calculation. Nevertheless, after geometric optimization, the two fragments ($CH_3$ and $CH_2$) on the sorbent surface are prone to motion to restore the initial microstructure of $H_3C$-$CH_3$ or $H_2C$=$CH_2$, which indicates that the oxidative C-C bond cleavage for $H_3C$-$CH_3$ and $H_2C$=$CH_2$ are difficult to occur. On the other hand, the HC≡CH bond cleavage is much easier to be activated on the sorbent surface, so as to result in $CO_x$ formation. These findings are consistent with the previous results of ethane successive dissociation on Fe surface [8]. With this respect, the first $C_2H_4$ dehydrogenation step is chosen as an indicator for deep oxidations (associated with $CO_x$ formation) of ethane in the current work.

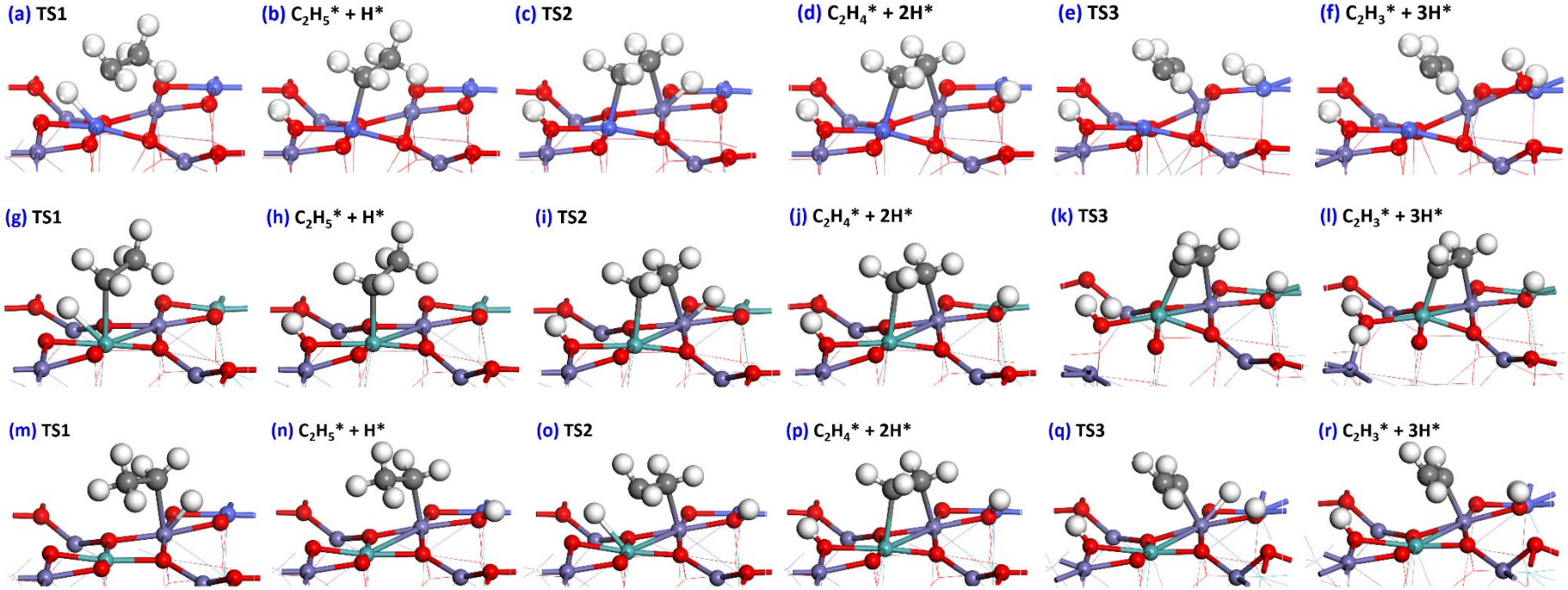


**Figure S10** The corresponding structures of $C_2H_6$ successive dehydrogenation on the surface of (a-f) $CoFe_2O_4$, (g-l) $MoFe_2O_4$, and (m-r) $Co_{1/4}Mo_{3/4}Fe_2O_4$, respectively.

## References


1. Liu, F.; Dai, J.; Liu, J.; Yang, Y.; Fang, R., Density Functional Theory Study on the Reaction Mechanism of Spinel $CoFe_2O_4$ with CO during Chemical-Looping Combustion. *The Journal of Physical Chemistry C* **2019,** 123, (28), 17335-17342, DOI 10.1021/acs.jpcc.9b03826.

2. Liu, F.; Liu, J.; Yang, Y.; Wang, Z.; Zheng, C., Reaction mechanism of spinel $CuFe_2O_4$ with CO during chemical-looping combustion: An experimental and theoretical study. *Proceedings of the Combustion Institute* **2019,** 37, (4), 4399-4408, DOI 10.1016/j.proci.2018.06.222.

3. Zheng, H.; Wang, J.; Lofland, S. E.; Ma, Z.; Mohaddes-Ardabili, L.; Zhao, T.; Salamanca-Riba, L.; Shinde, S. R.; Ogale, S. B.; Bai, F.; Viehland, D.; Jia, Y.; Schlom, D. G.; Wuttig, M.; Roytburd, A.; Ramesh, R., Multiferroic $BaTiO_3$-$CoFe_2O_4$ Nanostructures. *Science* **2004,** 303, (5658), 661, DOI 10.1126/science.1094207.

4. Zhao, H.; Tian, X.; Ma, J.; Chen, X.; Su, M.; Zheng, C.; Wang, Y., Chemical Looping Combustion of Coal in China: Comprehensive Progress, Remaining Challenges, and Potential Opportunities. *Energy & Fuels* **2020,** 34, (6), 6696-6734, DOI 10.1021/acs.energyfuels.0c00989.

5. Katayama, T.; Kurauchi, Y.; Mo, S.; Gu, K.; Chikamatsu, A.; Galiullina, L.; Hasegawa, T., p-Type Conductivity and Room-Temperature Ferrimagnetism in Spinel $MoFe_2O_4$ Epitaxial Thin Film. *Crystal Growth & Design* **2019,** 19, (2), 902-906, DOI 10.1021/acs.cgd.8b01454.

6. Abe, M.; Kawachi, M.; Nomura, S., X-ray and neutron diffraction studies in spinel $Fe_2MoO_4$. *Journal of the Physical Society of Japan* **1972,** 33, (5), 1296-1302, DOI 10.1143/JPSJ.33.1296.

7. Tang, Y.-M.; Yang, W.-Z.; Yin, X.-S.; Liu, Y.; Wan, R.; Wang, J.-T., Phenyl-substituted amino thiadiazoles as corrosion inhibitors for copper in 0.5M $H_2SO_4$. *Materials Chemistry and Physics* **2009,** 116, (2), 479-483, DOI 10.1016/j.matchemphys.2009.04.018.

8. Li, T.; Wen, X.; Li, Y.-W.; Jiao, H., Successive Dissociation of CO, $CH_4$, $C_2H_6$, and $CH_3CHO$ on Fe(110): Retrosynthetic Understanding of FTS Mechanism. *The Journal of Physical Chemistry C* **2018,** 122, (50), 28846-28855, DOI 10.1021/acs.jpcc.8b10310.